PHYSICS

Geometric phase amplification in a clock interferometer for enhanced metrology

Zhifan Zhou^{1,2}, Sebastian C. Carrasco³*, Christian Sanner⁴*, Vladimir S. Malinovsky³, Ron Folman²*

High-precision measurements are crucial for testing the fundamental laws of nature and advancing the technological frontier. Clock interferometry, where particles with an internal clock are coherently split and recombined along two spatial paths, has sparked interest due to its fundamental implications, especially at the intersection of quantum mechanics and general relativity. Here, we demonstrate that a clock interferometer provides metrological improvement compared to its technical noise–limited counterpart using a single internal quantum state. This enhancement around a critical working point can be interpreted as a geometric phase–induced signal-to-noise ratio gain. In our experimental setup, we infer a sensitivity enhancement of 8.8 decibels when measuring a small difference between external fields. We estimate that tens of decibels of sensitivity enhancement could be attained for measurements with a higher atom flux. This opens the door to developing a superior probe for fundamental physics and a high-performance sensor for various technological applications.

Copyright © 2025 The Authors, some rights reserved; exclusive licensee American Association for the Advancement of Science. No claim to original U.S.
Government Works.
Distributed under a Creative Commons Attribution
NonCommercial
License 4.0 (CC BY-NC).

INTRODUCTION

Matter-wave interferometry has evolved into a robust platform for probing the fundamental principles of quantum mechanics (1, 2). It is instrumental in sensing gravitational signals (1), testing the quantum superposition principle (3), and in exploring the intersection between quantum mechanics and general relativity (4–11). Furthermore, matter-wave interferometry is a fundamental demonstration of our ability to manipulate atomic motion coherently (2, 12, 13). A typical matter-wave interferometry experiment involves the creation of superposition of separated atomic wave packets, acquisition of a relative phase signal between them, subsequent interference of the wave packets, and some form of measurement of the final signal (in our case, a phase shift of the spatial interference pattern). Naturally, these operations contribute to the experimental noise budget, pushing the sensitivity away from the standard quantum limit (SQL), the lower sensitivity bound of metrology without quantum entanglement. Here, we use the internal structure of two-level atom matter waves and a steep change in the geometric phase (GP) response [rooted in the Pancharatnam-Berry phase (14-16)] to amplify a small interferometric signal. The primary advantage of the scheme appears in the observation that the technical noise is not amplified with the interferometric signal, thus increasing the overall signal-to-noise ratio. Moreover, our approach is an example of clock interferometry that exploits an interplay of internal (clock) and external (spatial) degrees of freedom (6, 10). Our study is a proof-ofprinciple experiment highlighting the potential of GP amplification for a wide range of precision measurements.

In a traditional atom interferometer, the interrogation signal is typically accumulated as a dynamical phase (DP), which is influenced by noise during the preparation, interrogation, and signal detection stages. The present work provides an experimental

demonstration of a relatively large enhancement in metrological sensitivity, 8.8 dB, through the Pancharatnam GP (14-16) compared to the case without GP amplification. The enhancement comes from an amplification of the signal response (phase shift of the interference pattern caused by an external field signal) around the critical working point, which is accompanied by an increase in quantum noise. The signal-to-noise ratio increases relative to the case without amplification because only the quantum noise increases, and the technical noise remains the same. The technique involves not only a separation of the atoms into two arms but also a superposition of internal states, called clock interferometry (4-11). The separation between the arms allows us to probe and compare different parts of the space, while the subsequent interference of two wave packets in different internal states gives rise to a Pancharatnam GP. The universality of the approach allows direct application of the technique to other atom interferometer schemes [atomic fountains (3), waveguides (17), fully trapped interferometers (13), etc.], and general quantum sensing platforms (12).

RESULTS

Model

We start by describing the matter-wave interferometry scheme we use. First, we prepare the system in a superposition of two spatially separated wave packets **A** and **B**. These wave packets are internally initialized via a radio frequency (RF) field to the appropriate two-level superposition. Then, a magnetic gradient is applied, and each wave packet experiences a different magnetic field. As wave packets evolve during the interrogation stage, each internal degree of freedom accumulates a differential phase due to the different coupling with the field (see Fig. 1E). For notational simplicity, we map the relative phase accumulation into wave packet **B**. We can then describe the wave packets by the following wave functions

$$\Psi_{\mathbf{A}} = \Psi_{\mathbf{A}}(\vec{r}) | a \rangle = \Psi_{\mathbf{A}}(\vec{r}) \left(\cos \frac{\theta}{2} | 2 \rangle + \sin \frac{\theta}{2} | 1 \rangle \right),
\Psi_{\mathbf{B}} = \Psi_{\mathbf{B}}(\vec{r}) | b \rangle = \Psi_{\mathbf{B}}(\vec{r}) \left(e^{i\phi_2} \cos \frac{\theta}{2} | 2 \rangle + e^{i\phi_1} \sin \frac{\theta}{2} | 1 \rangle \right)$$
(1)

¹Joint Quantum Institute, National Institute of Standards and Technology and the University of Maryland, College Park, MD 20742, USA. ²Department of Physics, Ben-Gurion University of the Negev, Beer-Sheva 84105, Israel. ³DEVCOM Army Research Laboratory, Adelphi, MD 20783, USA. ⁴Department of Physics, Colorado State University, Fort Collins, CO 80523, USA.

^{*}Corresponding author. Email: seba.carrasco.m@gmail.com (S.C.C.); sanner@colostate.edu (C.S.); folman@bgu.ac.il (R.F.)

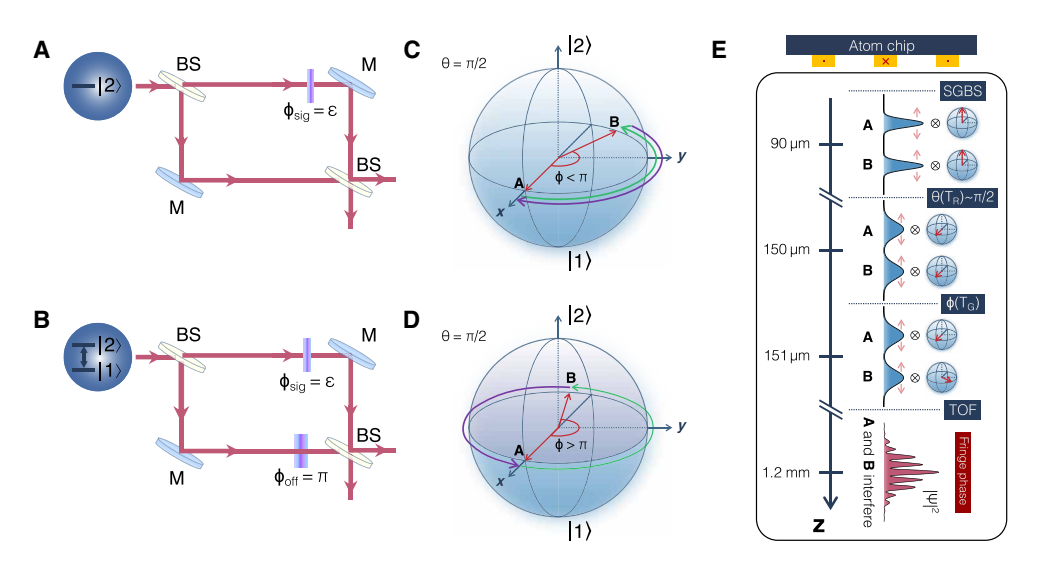


Fig. 1. Illustration of the matter-wave experimental sequence that gives rise to the GP amplification. In (A), we show the case in which there is the same single state in each arm, where $φ_{sig}$ is a weak interferometric signal due to the coupling to the external field. In (B), we present the case in which the matter wave is prepared in an internal superposition of the states |1⟩ and |2⟩. In (C), we illustrate that when the relative rotation of the Bloch vector is less than π, the geodesic connection line matches the latitude line, yielding no enclosed areas and thus a GP of zero. Conversely, when the relative rotation of the Bloch vector surpasses π [illustrated in (D)], the geodesic and latitude lines encircle the north hemisphere, leading to a GP shift of π when θ is π/2. In (E), we display the experimental realization of the sequence for the longitudinal interferometer (illustration not to scale). The experiment unfolds in free fall along the z axis, representing gravity's direction. Initially, we achieve a coherent spatial splitting using a Stern-Gerlach beam splitter (SGBS) (20) combined with a stopping pulse. This creates two wave packets in the |2⟩ state. We initialize the internal superposition using an RF pulse lasting T_R . Following this, we can encode a relative phase of the two wave packets by applying a magnetic field gradient ∂B/∂z for a duration of T_G . The final interference pattern, from which we derive the interference phase, forms during the time-of-flight (TOF) free evolution as the wave packets expand and overlap.

where $\psi_A(\vec{r})$ and $\psi_B(\vec{r})$ are the spatial components of the wave functions, $|1\rangle$ and $|2\rangle$ are two internal degrees of freedom that form the internal superposition, and ϕ_1 and ϕ_2 are the accumulated phases. Upon expansion, the Gaussian wave packets overlap and merge into a single wave packet, and the observed interference pattern takes the form (see derivation in Materials and Methods)

$$\rho(z) = \frac{1}{2} \langle \Psi_{\mathbf{A}} + \Psi_{\mathbf{B}} | \Psi_{\mathbf{A}} + \Psi_{\mathbf{B}} \rangle \propto \exp\left(-\frac{z^2}{2\sigma_z^2}\right)$$

$$\left\{1 + v\cos\left[\frac{2\pi}{\lambda}z + \Phi_T\right]\right\}$$
(2)

where λ is the spatial periodicity of the fringes, σ_z is the Gaussian width of the combined wave packet obtained after the time of flight, ν corresponds to visibility and

$$\Phi_{T} = \arg\langle a \mid b \rangle
= \phi_{2} + \arctan\left\{ \frac{\sin^{2}(\theta/2)\sin(\phi_{1} - \phi_{2})}{\cos^{2}(\theta/2) + \sin^{2}(\theta/2)\cos(\phi_{1} - \phi_{2})} \right\}$$
(3)

Thus, the phases φ_1 and φ_2 lead to a phase shift in the interference pattern. If $\theta=0$, the entire population is in state $|2\rangle$, and $\Phi_T=\varphi_2$. Similarly, if $\theta=\pi$, the entire population is in state $|1\rangle$ and $\Phi_T=\varphi_1$. In the limit $\varphi=\varphi_2-\varphi_1=\pi+\varepsilon$ with $\varepsilon\ll 1$, we obtain an approximated linear dependence given by

$$\Phi_T = \phi_2 - G\varepsilon \tag{4}$$

where $G = (1-R)^{-1}$ is the slope and $R = \cos^2(\theta/2)/\sin^2(\theta/2)$ is the ratio between the populations in the internal degrees of freedom. In the regime where R is approximately 1 (or $\theta \approx \pi/2$), the signal is boosted by G, and the interference visibility ν approaches

zero, following the equality: $v^2 = 1 - 4\sin^2(\theta/2)\cos^2(\theta/2)\sin^2(\phi/2)$ (see Materials and Methods). To bring the system to the working point ($\phi \approx \pi$), the introduction of a π phase offset is needed. To do that, additional manipulations can be used, such as the coherent coupling to additional levels discussed in (18). This places the system at the optimal sensitivity point for practical operation, that is, to estimate ϕ through a Φ_T measurement. Figure 1 (A and B) shows the interferometric scheme for two different cases. Figure 1A shows the case where $\theta = 0$, while Fig. 1B illustrates the case where θ is close to $\pi/2$; the phase is biased at π , and there is phase amplification.

GP amplification regime and metrological improvement

At first glance, one may argue that interferometry in the lowvisibility region presented in Fig. 1B would be impractical as the phase uncertainty diverges for $\nu \to 0$. As shown in the following, this region shows a metrological improvement compared to $\theta = 0$ or $\theta = \pi$, where the internal degrees of freedom do not play an active role since only one internal state is populated. Two conditions have to be met to obtain metrological improvement. First, ϕ has to be close to π , which is the working point of the interferometer. Second, θ must be close enough to $\pi/2$ to increase the signal but not precisely $\pi/2$, where the visibility is zero. Once these two conditions are satisfied, the phase uncertainty will not diverge, and the phase response will be amplified (as shown in Eq. 4) without a proportional increase in technical noise. This can effectively suppress the negative effect of technical noise on interferometric sensitivity. Typical matter-wave interferometers suffer from technical noise due to initial preparation, path length noise rooted in driving field noise, detection noise due to the limited resolution of the camera, and environmental noise, among others (1). This technical noise becomes more important when the number of atoms increases, as the quantum noise decreases (19).

Experimental scheme

Figure 1E depicts the experimental scheme [see more details in (10, 16)]. First, we prepare a Bose-Einstein condensate (BEC) with rubidium-87 atoms in the internal state $|2\rangle \equiv |F = 2, m_F = 2\rangle$, where F represents the total angular momentum and m_F its magnetic projection. After that, the wave packet is split into two using a Stern-Gerlach-type beam splitter technique (20). We then apply a uniform RF pulse to drive the population to state $|1\rangle \equiv |F=2, m_F=1\rangle$. Now, the internal states of both wave packets are a superposition of $|2\rangle$ and $|1\rangle$ with a polar angle θ (point **A** on the Bloch spheres in Fig. 1, C and D). We next apply a magnetic-field gradient; thus, both wave packets evolve under different magnetic fields. Because of the differing magnetic projections of $|1\rangle$ and $|2\rangle$, the wave packet rotates in the Bloch spheres until it points at **B** on the Bloch spheres (Fig. 1, C and D). Note that at this point, we have the wave packets that Eq. 1 describes. Last, the wave packets overlap through time-of-flight expansion, and visibility ν and phase Φ_T can be extracted by fitting the interference pattern to Eq. 2 [see Materials and Methods and (20)]. If θ is close enough to π / 2, we expect a phase amplification effect as Eq. 4 predicts.

We can understand phase-shift amplification in a GP picture using the geodesic rule proposition (16, 21, 22). The measured phase has two components. One part is the GP, which results from noncyclic evolution as in Fig. 1, C and D, and the other is a DP, a linear component resulting from magnetic projection. To be precise, $\Phi_T = \Phi_G + \Phi_D$, where the first term is the GP, and the other, the DP, is given by $\Phi_D = \phi(1 - \cos\theta)/2$. The GP follows the geodesic rule that dictates the reverse progression along the geodesic curve, which is the shortest path on the surface of the Bloch or Poincaré sphere, linking the initial and final points. The GP is half the area enclosed by the trajectory and the corresponding geodesic path. For instance, when the internal states of A and B are in an equal superposition, the Bloch vectors are on the equator of the Bloch sphere. If the relative rotation or azimuth angle between **A** and **B** is less than π , the geodesic and latitude lines coincide; therefore, they do not enclose any actual area (as shown in Fig. 1C). In contrast, when this rotation exceeds π , they collectively encompass a hemisphere (Fig. 1D), resulting in a geometric π phase change. If θ is not equal to $\pi/2$ but close, there is no sudden phase change but a region with increased slope. This geometric π phase change has been experimentally demonstrated in recent studies (16) and is related to the Pancharatnam phase (15). However, the metrological properties have never previously been analyzed in detail. Notably, the GP depends only on the parameter-space area. Thus, our scheme is, by design, resilient to certain disturbances and imperfections. This GP resilience has been studied both theoretically and experimentally in spin-half systems with cyclic evolutions (23-28). In the broader context of noncyclic evolution, we observed the rapid phase change along the geodesic rule, the amplification of a small phase change signal, and the lack of amplification of technical noise. Thus, the hindering effect of technical noise on interferometric sensitivity is expected to be suppressed.

Observation of a magnified phase shift and sensitivity improvement

Figure 2 depicts the main experimental results. Each data point is an average of eight experimental cycles. The small data sample shows

that the method works well without requiring prohibitively large data samples. As can be seen from the fit errors in fig. S1, single shots would be enough for some applications. In Fig. 2A, the red circles show a rapid phase change when 51.4 and 48.6% of the population (with a 0.4% SEM) is in states |2\rangle and |1\rangle, respectively. The population of 51.4% is about 3 SEM and 1 SD from an equal partition. Here, ϕ is scanned around the working point $\phi = \pi$, as suggested by the theoretical model. In contrast, the green and blue circles illustrate the case where the population is in state $|1\rangle$ or $|2\rangle$. Thus, a conventional phase measurement from a single-state interference follows a linear phase accumulation process without amplification. Figure 2A also displays the SEM of the measured interferometric phase, which increases slightly around the working point. Taking into account the increase in slope and noise, we estimate within the steep slope region an improvement in the measurement sensitivity of 8.8 dB compared to the best conventional counterpart (interferometry with |2\) experiencing the same noise floor. The direct comparison of the four data points connected by black dashed lines in Fig. 2A is highlighted in Fig. 2C (see the detailed sensitivity calculation in the Supplementary Materials). Figure 2B illustrates the geometric character of phase amplification by removing the DP to isolate the GP. The phase remains rigid until it changes rapidly around $\phi = \pi$. Figure 2D presents the analytical results for the interference phase across various population distributions, predicting the phase change depicted in Fig. 2A.

To better understand the reason for the metrological improvement, we explain how phase measurement noise depends on ϕ in Fig. 2A. When ϕ approaches π (see Fig. 3A), the visibility slowly diminishes following theory, $v^2 = 1 - 4\sin^2(\theta/2)\cos^2(\theta/2)\sin^2(\phi/2)$ (9, 10). In an interferometer only limited by quantum noise, the theory predicts an increase in phase measurement noise proportional to 1/v as the extraction of the low-visibility phase becomes more difficult. However, practical matter-wave interferometer implementations suffer from additional technical noise sources. Figure 3B plots measured phase error as a function of visibility (red circles) together with two theoretical models. The solid blue line shows the 1/v scaling in the phase error that one would expect for an interferometer to operate at the SQL. The dashed red line shows the same model with the addition of a technical noise of 0.1 rad. This modification of the 1 / v model agrees well with the data points that show the dependence of the phase measurement uncertainty with respect to the visibility (see Fig. 3B). Note that as $\theta \neq \pi/2$, the divergent part of Fig. 3B is unreachable as there is a minimum visibility value (highlighted in both panels).

Accordingly, the uncertainty for the phase measurement has two components: fundamental atom shot noise or quantum noise that scales with the reduction in visibility, and technical noise, $\Delta\Phi_T^2 = \Delta\Phi_{\rm quantum}^2 + \Delta\Phi_{\rm technical}^2.$ The measurement uncertainty for phase φ , which is the minimal phase that can be resolved, is given by

$$\Delta \phi = \frac{\Delta \Phi_T}{|\partial \Phi_T / \partial \phi|} \tag{5}$$

For large enough values of $G = \partial \Phi_T / \partial \Phi$, the technical noise does not contribute considerably to the sensitivity and $\Delta \Phi \approx \Delta \Phi_{\rm quantum} / G$. In that case, only quantum noise limits the sensitivity. In contrast, when using one internal state, the technical noise limits the sensitivity. We offer a derivation of Eq. 5 in the Supplementary Materials.

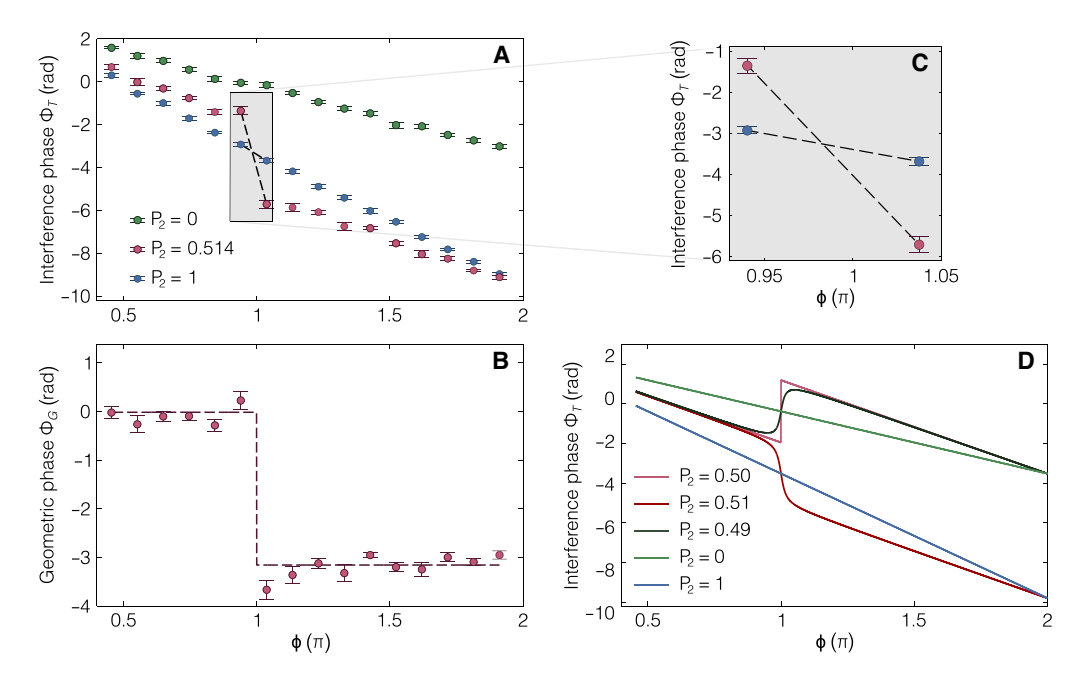


Fig. 2. Experimental results of the GP enhancement. In (**A**), we measure the interference phase (red circles) when each wave packet is prepared with 51.4 and 48.6% (and 0.4% uncertainty) of the population in states |2⟩ and |1⟩, respectively. In green and blue circles, phase measurements using single-state interference demonstrate linear phase accumulation. Each data point is an average of eight experimental cycles, and the error bars are the SEM in this subsample. In (**B**), we remove the DP (estimated analytically from the population distribution in state |2⟩) to illustrate the geometric nature of the phase amplification. We compute the dashed purple curve using $Φ_G = Φ_T - Φ_D$, according to the analytical expressions in the main text. In (A) and (B), we choose the appropriate reference phase so that the GP starts at zero, thus matching the geodesic rule. In (**C**), we gather the two pairs of data points that will be used to calculate the corresponding sensitivities. The raw data for four single shots, representing these four data points, are shown in fig. S1. We connect each pair of points with a black dashed line as in (A). We obtain 8.8 dB of enhancement in our $Δφ^2$ sensitivity estimation. Note that the enhancement comes primarily from the phase amplification that overcomes the minor uncertainty increase (see the discussion accompanying Fig. 3). In (**D**), we display model traces illustrating the transition from single-state to two-state interference, exhibiting the phase amplification.

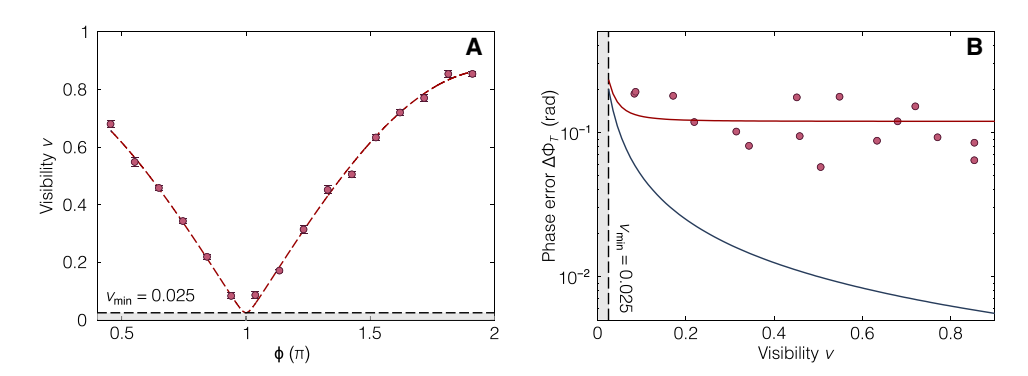
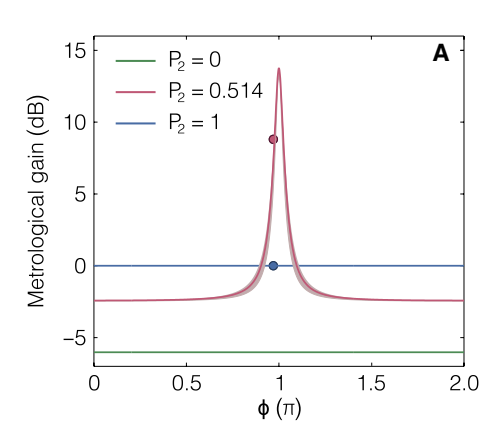


Fig. 3. Visibility and measurement uncertainty. In (A), we display the visibility of the interference pattern as a function of the relative rotation. The populations in the $|2\rangle$ and $|1\rangle$ states are measured as 51.4 and 48.6%. The states are not equally populated, and, therefore, the visibility does not reach zero. Instead, the minimal visibility is 0.025 (see main text). Each data point is an average of eight experimental cycles, and the error bars are the SEM in this subsample. In (B), we present how the phase error (SEM) varies as a function of visibility. The data suggest that the measured phase fluctuations do not change over a wide visibility range, which is expected when technical noise is the dominant contribution. The red line is derived from a straightforward model where a constant technical noise of approximately 0.1 rad is added to a quantum noise component (blue line), which varies as $\left(v - \sqrt{N} - \sqrt{A}\right)^{-1}$, where v is the visibility, N is the atom number of 5×10^3 , and A is the number of experimental cycles (eight). Note that the phase error of the data reaches 0.2 rad at low visibility, consistent with the \pm 0.2 rad presented in Fig. 2C.

Comparison with theoretical predictions

Figure 4A shows how the estimated metrological gain depends on the relative rotation φ for selected values of the population in states $|1\rangle$ and $|2\rangle$. To calculate this, we compute the phase change uncertainty as a function of φ using the model $\Delta\Phi_T^2=\left(\nu\sqrt{NA}\right)^{-2}+\Phi_{\rm technical}^2$

which agrees with the experimental data previously discussed. In addition, we evaluate the slope $G = \partial \Phi_T / \partial \phi$ from Eq. 3. As a reference to define the metrological gain, we use the measurement uncertainty for phase ϕ obtained when operating the interferometer at $P_2 = 1$ (the black pentagon in Fig. 4A). We estimate a metrological gain of approximately 10 dB around the working point $\phi = \pi$ when $P_2 = 0.514$.



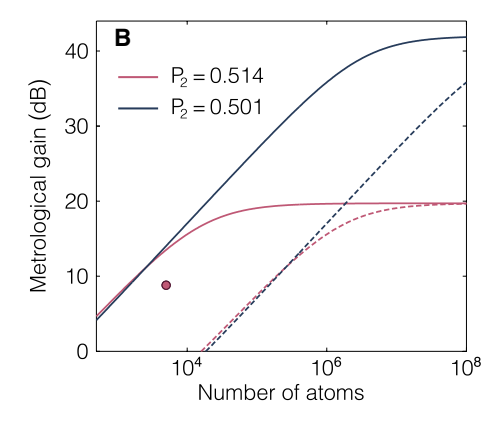


Fig. 4. Metrological gain with different experimental parameters. In (**A**), we present the estimated metrological gain, $\Delta \varphi(P_2 = 0.514) / \Delta \varphi(P_2 = 1)$, with respect to the standard single-state interferometer (the entire population in state |2), $P_2 = 1$) versus the relative rotation φ . The red point represents the experimental measurement of 8.8 dB when $P_2 = 0.514$ and $\varphi \simeq \pi$, while the blue point represents the reference value $P_2 = 1$. We perform both measurements using $N = 5 \times 10^3$ atoms. The red, blue, and green solid curves indicate the theoretical prediction when $P_2 = 0.514$, $P_2 = 1$, and $P_2 = 0$, respectively, assuming a technical noise of 0.1 rad. Because of the state's different magnetic projections, the last two differ by 6 dB. The gray area around the red solid curve represents the results when considering a 0.4% uncertainty in the internal populations. Another uncertainty source is the magnetic gradient fluctuations that we estimate to give rise to a 2% uncertainty in φ (smaller than the data points width), consistent with previous calculations [specifically in (20, 45); see the Supplementary Materials]. In (**B**), we show the estimated metrological gain, relative to the $P_2 = 1$ case, as a function of the number of atoms N. The red and blue solid curves represent the cases where $P_2 = 0.514$ and $P_2 = 0.501$, and $\varphi = \pi$. The latter generates higher metrological gain due to a higher phase-change slope, as pointed out in Eq. 3. Note that the experimental point is lower than the theoretical curve as it was not taken exactly at $\varphi = \pi$. All solid curves involve an estimated technical noise of 0.1 rad, which is realistic for a miniaturized apparatus (39, 46). Dashed curves show the prediction for a technical noise of 0.01 rad.

That value is close to 8.8 dB extracted from the experimental results (the red star in Fig. 4A). We attribute the difference to an underestimation of the slope due to the lack of sampling resolution in the vicinity of the working point. For reference, we also include a plot of the expected results using a single quantum state, for $P_2=0$ and $P_2=1$, which differ because of the difference in the magnetic projection between states.

In the low atom flux limit, the quantum noise is relatively large (29). This limits the metrological gain that can be achieved by GP amplification. We anticipate that a high-flux atom interferometer (19) will alleviate this limit and increase the impact of the GP amplification. In Fig. 4B, we show how the metrological gain increases with N. Furthermore, if N is large and the population ratio is closer to one (see the $P_2=0.501$ case), the metrological gain could be even higher (up to 40 dB in the blue solid curve) because of a steeper phase response. We assume that the technical noise is the same (0.1 rad) when calculating these predictions. In Fig. 4B, we also include dashed black and red curves showing the prediction of a technical noise of 0.01 rad as an example of what happens with smaller values of technical noise. In this case, our technique still offers metrological improvement. However, the atom flux threshold upon which we start to observe it increases.

DISCUSSION

We have demonstrated that atom interferometry using matter waves with internal degrees of freedom (so-called clock interferometry) can be metrologically advantageous. This improvement is due to the GP amplification that arises from noncyclic evolution, which results in a steep phase response that is not accompanied by a proportional rise in noise. We experimentally demonstrated 8.8-dB metrological improvement compared to the case without GP amplification. We estimate that tens of decibels of enhancement could be attained by increasing the atom flux and adjusting the ratio between the internal states. Since long lifetime clock transitions have been used for

matter-wave interferometry (30), we anticipate that our scheme would offer substantial capabilities in pushing the limits of matterwave sensing capabilities (3, 31). In summary, this work offers insights into the potential of GP amplification to boost metrological sensitivity and may be implemented in numerous applications.

As an outlook, let us emphasize that this work should be regarded as a proof-of-principle experiment highlighting opportunities for progress in sensors based on the noncyclic evolution adhering to the geodesic rule. An additional advantage not discussed here is the potential for fast phase accumulation due to the possibility of nonadiabatic GP accumulation (32-34). Further development is required to adapt this method to different physical observables that one would like to measure, where any observable that changes the "tick rate" of the clock by a differential interaction with its two levels may be detected, e.g., dc and ac Stark shifts, if there exists a gradient across the interferometer. For example, one may envision the magnetic gradient used in this work as analogous (6, 10) to a difference in proper time that a gravitational field would produce and our technique as comparing the tick rates of a quantum clock (represented by the internal states) in a spatial superposition (probing two regions of space). Therefore, the experimental scheme could work as a gravitational sensor if highprecision clocks capable of resolving the redshift are used (35, 36). Thus, the technique introduced here may be suitable for studying the interplay between general relativity and quantum mechanics [and potentially testing exotic concepts such as the discreteness of time (37)]. Last, the method described here can be combined with other quantum noise reduction technologies, such as spin squeezing (38).

MATERIALS AND METHODS

Detailed experimental scheme

In Fig. 5, we present the details of our experimental procedure. This includes the splitting of a single BEC wave packet into a pair in different locations (steps 1 to 3), the halt of their mutual velocity (step 4),

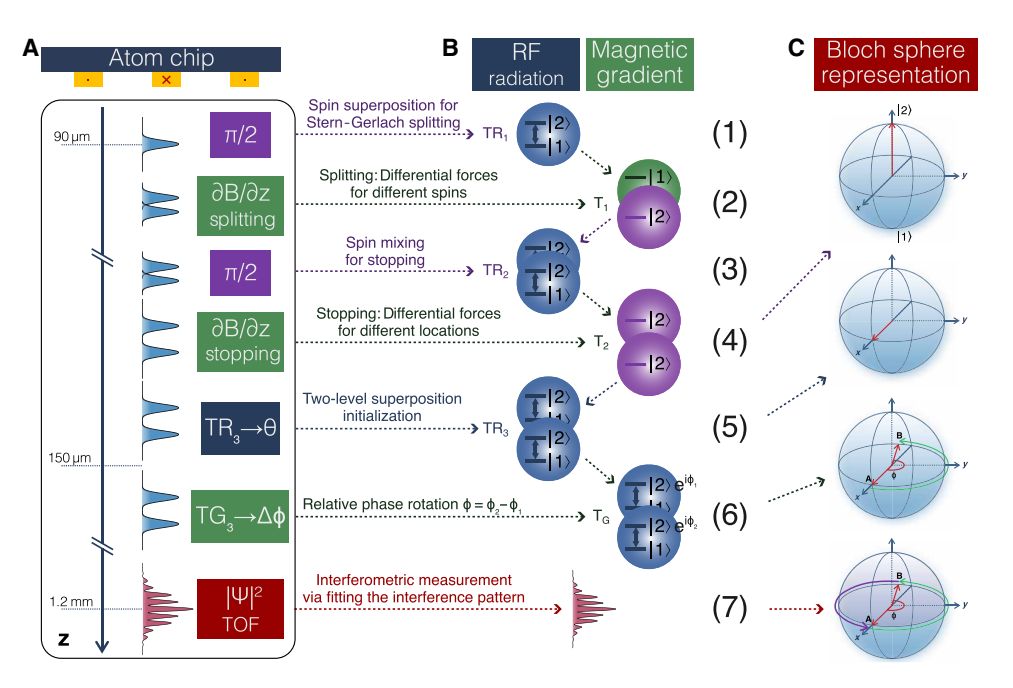


Fig. 5. Detailed scheme of the clock interferometer. In (**A**), we show the full experimental sequence, depicted schematically (not to scale). The experiment takes place in free fall along the z axis. In (**B**), we present the evolution of the states along the sequence. After releasing the atoms from the trap, one RF $\pi/2$ pulse (TR_1) creates an equal superposition of the $|2\rangle \equiv |F = 2$, $m_F = 2\rangle$ and $|1\rangle \equiv |F = 2$, $m_F = 1\rangle$ states (step 1). These two spin states are then exposed to a differential force created by a magnetic gradient pulse $\partial B/\partial z$ of duration T_1 (step 2), leading each state to different positions and velocities. A second $\pi/2$ pulse (TR_2) (step 3) mixes the spins in each wave packet. Then, a second magnetic gradient pulse (TR_2) (step 4) yields differential forces again to stop the wave packets. During TR_2 , the wave packets'|1\rangle state component is pushed outside the experimental zone. The system then consists of two wave packets in the $|2\rangle$ state (separated along the z axis, with zero relative velocity) as in the beginning of Fig. 1E. Last, the experiment unfolds following Fig. 1E description (here steps 5, 6, and 7). In (**C**), we show the states' evolution on the Bloch sphere's surface during the sequence. After preparing two coherent wave packets at distinct locations (step 4), an RF pulse of duration TR_3 (TR_3 in Fig. 1) is applied to shift the two vectors from the north pole to the equatorial plane of the Bloch sphere to initialize the internal superposition (step 5). A magnetic field gradient of duration TR_3 induces the relative phase Φ (step 6), and the interferometric measurement is done via fitting the interference pattern (step 7).

the initiation of a two-level superposition inside each wave packet (step 5), the introduction of a relative phase (step 6), and the generation of an interference pattern during the time-of-flight process (step 7). Our experiment leverages an atom chip setup as discussed in the literature in (39). We start by establishing a BEC composed of approximately 10^4 rubidium-87 atoms in the state $|2\rangle \equiv |F=2, m_F=2\rangle$. This BEC is roughly 90 μ m beneath the chip surface in a magnetic trap. After releasing the BEC atoms from the trap, the entire experimental sequence occurs in a homogeneous magnetic bias field of 36.7 G in the direction y (with z being the direction of gravity). This field establishes an effective two-level system, with $|1\rangle \equiv |F=2, m_F=1\rangle$ and $|2\rangle \equiv |F=2, m_F=2\rangle$, through the nonlinear Zeeman effect. Here, $E_{ij}=E_{21}$ is approximately $h\times25$ MHz (where i and j are the values of m_F , all within the F=2 manifold, and h is the Planck constant), and $E_{21}-E_{10}$ is approximately $h\times180$ kHz.

Next, we introduce an RF pulse with a typical duration of $10~\mu s$, resulting in a rotation of $\theta = \pi/2$. This prepares a spin superposition, $(|1\rangle+|2\rangle)/\sqrt{2}$, between the $|2\rangle$ and $|1\rangle$ states. Then, a magnetic gradient pulse, represented as $\partial B/\partial z$ and lasting $T_1=4~\mu s$, is applied. This pulse, produced by currents in the atom-chip wires, facilitates Stern-Gerlach splitting, where different spins experience differential forces. To enable interference between the two wave packets (given $|2\rangle$ and $|1\rangle$ are orthogonal), a second $\pi/2$ pulse (TR_2) is applied to mix the spins. To stop the relative velocity of the wave packets, a subsequent magnetic gradient pulse (T_2) is used. This generates differential forces for the same-spin states positioned differently. A spatial

superposition of two wave packets in state $|2\rangle$ now exists (separated along the z axis). Note that during T_2 , the $|1\rangle$ state of the two wave packets is expelled from the experimental region.

The θ control (introduced in Fig. 1A) is achieved using a third RF pulse with a duration of TR_3 (referred to as T_R when discussing Fig. 1). The relative rotation, ϕ , between the wave packets can be adjusted with a third magnetic field gradient, lasting T_G . The wave packets then undergo expansion and overlap to produce the interference pattern, with a time of flight of approximately 10 ms (substantially exceeding the reciprocal of the trap frequency, roughly 500 Hz). Last, we capture an image through absorption imaging (see fig. S3). We offer a simulation of the experimental procedure in the Supplementary Materials.

Generation of magnetic gradient pulses

Three parallel gold wires on the chip surface produce magnetic gradient pulses. These wires have a length of 10 mm, a width of 40 μm , and a thickness of 2 μm . The current of the chip wire is generated by a simple 12.5 V battery and is modulated using a homemade current shutter. The three parallel gold wires are spaced 100 μm apart (center to center), with the same current flowing through them in alternating directions. In contrast with using a single gold wire, this three-wire configuration creates a 2D quadrupole field at $z=100~\mu m$ below the atom chip. Given that magnetic field fluctuations are proportional to the field strength and the primary source of instability stems from the gradient pulses (since the bias fields from

external coils are highly stable), placing the atoms near the center (or zero point) of the quadrupole field effectively reduces the magnetic-field noise. This is achieved by the three-wire configuration while preserving the magnetic gradients' strength.

Interferometric phase extraction

As stated in the main text

$$\begin{split} \rho(z) &= \frac{1}{2} \langle \Psi_{\mathbf{A}} + \Psi_{\mathbf{B}} \mid \Psi_{\mathbf{A}} + \Psi_{\mathbf{B}} \rangle \\ &= \frac{1}{2} \mid \psi_{\mathbf{A}} \mid^2 + \frac{1}{2} \mid \psi_{\mathbf{B}} \mid^2 + \mid \overline{\psi}_{\mathbf{A}} \psi_{\mathbf{B}} \mid \mid \langle a \mid b \rangle \mid \cos(\arg \langle \Psi_{\mathbf{A}} \mid \Psi_{\mathbf{B}} \rangle) \end{split}$$
(6)

After the wave packets expand on the free space, the width of the spatial components, ψ_A and ψ_B , of the wave packets, **A** and **B**, becomes much bigger than the separation. Thus, $|\psi_A|^2$, $|\psi_B|^2$, and $\overline{\psi}_A\psi_B$ can be approximated by a Gaussian wave packet; consequently

$$\rho(z) = \mathcal{A} \exp \left[-\frac{z^2}{2\sigma_z^2} \right] \left\{ 1 + \nu \cos \left[\arg \langle \Psi_{\mathbf{A}} | \Psi_{\mathbf{B}} \rangle \right] \right\}$$
 (7)

where σ_z is the Gaussian width of the combined wave packet obtained after the time of flight, A a normalization constant, and ν corresponds to the visibility given by

$$v = |\langle a | b \rangle| = \sqrt{1 - 4\sin^2(\theta/2)\cos^2(\theta/2)\sin^2(\phi/2)}$$
 (8)

To calculate the interference pattern's spatial frequency and phase, we must consider that

$$\arg\langle \Psi_{\mathbf{A}} | \Psi_{\mathbf{B}} \rangle = \arg(\overline{\Psi}_{\mathbf{A}} \Psi_{\mathbf{B}}) + \arg\langle a | b \rangle \tag{9}$$

The term $\arg\langle a | b \rangle$ equals the total phase Φ_T and can be directly evaluated. To calculate $\arg(\overline{\psi}_A\psi_B)$, we must consider the time evolution of a Gaussian wave packet in free space

$$\Psi_{\text{free}}(z,t) = \left[\sqrt{2\pi\sigma^2}\alpha(t)\right]^{-1/2} \exp\left[-\frac{z^2}{4\alpha(t)\sigma^2}\right]$$
(10)

where $\alpha(t) = 1 + i \frac{\hbar t}{2m\sigma^2}$ describes the expansion of the wave packet after a time-of-flight t, m is the mass of a 87 Rb atom, and \hbar is the reduced Planck constant. We use this equation to evaluate the interference of two wave packets separated by d

$$\begin{split} \overline{\Psi}_{\mathbf{A}}\Psi_{\mathbf{B}} &= \overline{\Psi}_{\text{free}}(z+d/2,t)\Psi_{\text{free}}(z-d/2,t) \\ &= \left[\sqrt{2\pi\sigma^2} \left| \alpha(t) \right|^2 \right]^{-1/2} \exp\left[-\frac{(z-d/2)^2}{4\alpha(t)\sigma^2} - \frac{(z+d/2)^2}{4\overline{\alpha}(t)\sigma^2} \right] \end{split} \tag{11}$$

After a long evolution, $t \gg m\sigma^2 / \hbar$, we can approximate $\alpha \approx i \frac{\hbar t}{2m\sigma^2}$. In this limit

$$\arg(\overline{\psi}_{A}\psi_{B}) = \frac{md}{\hbar t}z \tag{12}$$

This leads to the expression

$$\arg \langle \Psi_{\mathbf{A}} | \Psi_{\mathbf{B}} \rangle = \frac{2\pi}{\lambda} z + \phi_2$$

$$+ \arctan \left\{ \frac{\sin^2(\theta/2)\sin(\phi_1 - \phi_2)}{\cos^2(\theta/2) + \sin^2(\theta/2)\cos(\phi_1 - \phi_2)} \right\}$$
(13)

with $\lambda = ht/(md)$. Last, combining Eq. 7 and Eq. 13, we reobtain Eq. 2

$$\rho(z) = \mathcal{A}\exp\left(-\frac{z^2}{2\sigma_z^2}\right) \left\{1 + \nu\cos\left[\frac{2\pi}{\lambda}z + \Phi_T\right]\right\}$$
 (14)

with $\sigma_{z}^{2} = \sigma^{2} |\alpha|^{2}$.

For absorption imaging, we assume that the wave packet is centered in $z_{\rm com}$ and an extra relative phase $2\pi z_{\rm ref}/\lambda$ (which shifts the phase by a fixed value), giving rise to the profile

$$n(z) = A \exp\left[-\frac{(z - z_{\text{com}})^2}{2\sigma_z^2}\right]$$

$$\left\{1 + v \sin\left[\frac{2\pi}{\lambda}(z - z_{\text{ref}}) + \Phi_T\right]\right\} + c$$
(15)

where c is the background optical density of the absorption imaging. Note that what we perform is not a state-selective measurement that distinguishes between the two internal states. Thus, the internal superposition can be measured properly, as each state is equally accounted for to form the final interference pattern.

We provide examples of this fit and further discuss fit errors in the Supplementary Materials. In particular, we show that the fit errors are consistent with what is expected by theory by comparing them with Monte Carlo simulations. We find that the fit error we obtain from the raw data is similar to the one expected from sampling the distribution with N atoms.

Alternative interpretations

Note that a mathematical analysis also supports an alternative explanation in which one interprets the experiment as beating two competing patterns [see (11)]. Although this interpretation is as valid as that regarding the GP, we find the latter to be more attractive when describing the origin of the steep slope. The reason is that the GP emerges naturally as a phase shift from the interference pattern. This interpretation is also easier to generalize to other contexts with no spatial pattern. Last, another interpretation of the results could be in terms of phase vortices (40–44). Equation 3 for the interferometric phase Φ_T exhibits a vortex when $\theta=\pi/2$ and $\varphi=\pi$. Consequently, Φ_T changes rapidly with respect to φ near the vortex, giving rise to the increasing slope.

We must also point out that similar amplification phenomena can occur in various physical situations. As an example, we provide an alternative description of a clock interferometer using plane waves in the Supplementary Materials.

Supplementary Materials

This PDF file includes:

Figs. S1 to S5 Supplementary Text

REFERENCES AND NOTES

- A. D. Cronin, J. Schmiedmayer, D. E. Pritchard, Optics and interferometry with atoms and molecules. Rev. Mod. Phys. 81, 1051–1129 (2009).
- 2. M. A. Kasevich, Coherence with atoms. Science 298, 1363–1368 (2002).
- T. Kovachy, P. Asenbaum, C. Overstreet, C. A. Donnelly, S. M. Dickerson, A. Sugarbaker, J. M. Hogan, M. A. Kasevich, Quantum superposition at the half-metre scale. *Nature* 528, 530–533 (2015).
- M. Zych, F. Costa, I. Pikovski, Č. Brukner, Quantum interferometric visibility as a witness of general relativistic proper time. Nat. Commun. 2, 505 (2011).
- S. Sinha, J. Samuel, Atom interferometry and the gravitational redshift. Class. Quantum Grav. 28, 145018 (2011)
- Y. Margalit, Z. Zhou, S. Machluf, D. Rohrlich, Y. Japha, R. Folman, A self-interfering clock as a "which path" witness. Science 349, 1205–1208 (2015).

SCIENCE ADVANCES | RESEARCH ARTICLE

- I. Pikovski, M. Zych, F. Costa, Č. Brukner, Universal decoherence due to gravitational time dilation. Nat. Phys. 11, 668–672 (2015).
- G. Rosi, G. D'Amico, L. Cacciapuoti, F. Sorrentino, M. Prevedelli, M. Zych, Č. Brukner, G. M. Tino, Quantum test of the equivalence principle for atoms in coherent superposition of internal energy states. *Nat. Commun.* 8, 15529 (2017).
- I. Pikovski, M. Zych, F. Costa, Č. Brukner, Time dilation in quantum systems and decoherence. New J. Phys. 19, 025011 (2017).
- Z. Zhou, Y. Margalit, D. Rohrlich, Y. Japha, R. Folman, Quantum complementarity of clocks in the context of general relativity. Class. Quantum Grav. 35, 185003 (2018).
- S. Loriani, A. Friedrich, C. Ufrecht, F. di Pumpo, S. Kleinert, S. Abend, N. Gaaloul, C. Meiners, C. Schubert, D. Tell, É. Wodey, M. Zych, W. Ertmer, A. Roura, D. Schlippert, W. P. Schleich, E. M. Rasel, E. Giese, Interference of clocks: A quantum twin paradox. Sci. Adv. 5, eaax8966 (2019).
- C. P. Koch, U. Boscain, T. Calarco, G. Dirr, S. Filipp, S. J. Glaser, R. Kosloff, S. Montangero, T. Schulte-Herbrüggen, D. Sugny, F. K. Wilhelm, Quantum optimal control in quantum technologies. Strategic report on current status, visions and goals for research in Europe. EPJ Quantum Technol. 9, 19 (2022).
- B. Dash, M. H. Goerz, A. Duspayev, S. C. Carrasco, V. S. Malinovsky, G. Raithel, Rotation sensing using tractor atom interferometry. AVS Quantum Sci. 6, 014407 (2024).
- M. V. Berry, Quantal phase factors accompanying adiabatic changes. Proc. R. Soc. Lond. A 392, 45–57 (1984).
- S. Pancharatnam, Generalized theory of interference, and its applications: Part I. Coherent pencils. Proc. Indian Acad. Sci. 44, 247–262 (1956).
- Z. Zhou, Y. Margalit, S. Moukouri, Y. Meir, R. Folman, An experimental test of the geodesic rule proposition for the noncyclic geometric phase. Sci. Adv. 6, eaay8345 (2020).
- C. D. Panda, M. Tao, J. Egelhoff, M. Ceja, V. Xu, H. Müller, Coherence limits in lattice atom interferometry at the one-minute scale. *Nat. Phys.* 20, 1234–1239 (2024).
- D. Jaksch, J. I. Cirac, P. Zoller, S. L. Rolston, R. Côté, M. D. Lukin, Fast quantum gates for neutral atoms. *Phys. Rev. Lett.* 85, 2208–2211 (2000).
- A. Herbst, T. Estrampes, H. Albers, V. Vollenkemper, K. Stolzenberg, S. Bode, E. Charron, E. M. Rasel, N. Gaaloul, D. Schlippert, High-flux source system for matter-wave interferometry exploiting tunable interactions. *Phys. Rev. Res.* 6, 013139 (2024).
- S. Machluf, Y. Japha, R. Folman, Coherent Stern-Gerlach momentum splitting on an atom chip. Nat. Commun. 4, 2424 (2013).
- J. Samuel, R. Bhandari, General setting for Berry's phase. Phys. Rev. Lett. 60, 2339–2342 (1988)
- 22. R. Bhandari, SU (2) phase jumps and geometric phases. *Phys. Lett. A* **157**, 221–225 (1991).
- A. Carollo, I. Fuentes-Guridi, M. F. Santos, V. Vedral, Geometric phase in open systems. Phys. Rev. Lett. 90, 160402 (2003).
- G. De Chiara, G. M. Palma, Berry phase for a spin 1/2 particle in a classical fluctuating field. Phys. Rev. Lett. 91, 090404 (2003).
- P. J. Leek, J. M. Fink, A. Blais, R. Bianchetti, M. Göppl, J. M. Gambetta, D. I. Schuster, L. Frunzio, R. J. Schoelkopf, A. Wallraff, Observation of Berry's phase in a solid-state qubit. Science 318, 1889–1892 (2007).
- S. Filipp, J. Klepp, Y. Hasegawa, C. Plonka-Spehr, U. Schmidt, P. Geltenbort, H. Rauch, Experimental demonstration of the stability of Berry's phase for a spin-1/2 particle. *Phys. Rev. Lett.* 102, 030404 (2009).
- S. Berger, M. Pechal, A. A. Abdumalikov, C. Eichler, L. Steffen, A. Fedorov, A. Wallraff,
 Filipp, Exploring the effect of noise on the Berry phase. *Phys. Rev. A* 87, 060303 (2013).
- C. G. Yale, F. J. Heremans, B. B. Zhou, A. Auer, G. Burkard, D. D. Awschalom, Optical manipulation of the Berry phase in a solid-state spin qubit. *Nat. Photonics* 10, 184–189 (2016).
- F. Anders, A. Idel, P. Feldmann, D. Bondarenko, S. Loriani, K. Lange, J. Peise, M. Gersemann, B. Meyer-Hoppe, S. Abend, N. Gaaloul, C. Schubert, D. Schlippert, L. Santos, E. Rasel, C. Klempt, Momentum entanglement for atom interferometry. *Phys. Rev. Lett.* 127, 140402 (2021).
- L. Hu, N. Poli, L. Salvi, G. M. Tino, Atom interferometry with the Sr optical clock transition. *Phys. Rev. Lett.* 119, 263601 (2017).
- C. Overstreet, P. Asenbaum, J. Curti, M. Kim, M. A. Kasevich, Observation of a gravitational Aharonov-Bohm effect. Science 375, 226–229 (2022).
- E. Sjöqvist, D. M. Tong, L. Mauritz Andersson, B. Hessmo, M. Johansson, K. Singh, Non-adiabatic holonomic quantum computation. New J. Phys. 14, 103035 (2012).
- 33. K. Xu, T. Xie, F. Shi, Z.-Y. Wang, X. Xu, P. Wang, Y. Wang, M. B. Plenio, J. Du, Breaking the quantum adiabatic speed limit by jumping along geodesics. *Sci. Adv.* **5**, aax3800 (2019).

- J. W. Zhang, L.-L. Yan, J. C. Li, G. Y. Ding, J. T. Bu, L. Chen, S.-L. Su, F. Zhou, M. Feng, Single-atom verification of the noise-resilient and fast characteristics of universal nonadiabatic noncyclic geometric quantum gates. *Phys. Rev. Lett.* 127, 030502 (2021).
- J. Rudolph, T. Wilkason, M. Nantel, H. Swan, C. M. Holland, Y. Jiang, B. E. Garber,
 P. Carman, J. M. Hogan, Large momentum transfer clock atom interferometry on the 689 nm intercombination line of strontium. *Phys. Rev. Lett.* 124, 083604 (2020).
- F. Di Pumpo, C. Ufrecht, A. Friedrich, E. Giese, W. P. Schleich, W. G. Unruh, Gravitational redshift tests with atomic clocks and atom interferometers. *PRX Quantum* 2, 040333 (2021)
- M. Christodoulou, A. Di Biagio, P. Martin-Dussaud, An experiment to test the discreteness of time. Quantum 6, 826 (2022).
- S. C. Carrasco, M. H. Goerz, Z. Li, S. Colombo, V. Vuletić, V. S. Malinovsky, Extreme spin squeezing via optimized one-axis twisting and rotations. *Phys. Rev. Appl.* 17, 064050 (2022)
- M. Keil, O. Amit, S. Zhou, D. Groswasser, Y. Japha, R. Folman, Fifteen years of cold matter on the atom chip: Promise, realizations, and prospects. J. Mod. Opt. 63, 1840–1885 (2016).
- S. Inouye, S. Gupta, T. Rosenband, A. P. Chikkatur, A. Görlitz, T. L. Gustavson,
 A. E. Leanhardt, D. E. Pritchard, W. Ketterle, Observation of vortex phase singularities in Bose-Einstein condensates. *Phys. Rev. Lett.* 87, 080402 (2001).
- A. E. Leanhardt, A. Görlitz, A. P. Chikkatur, D. Kielpinski, Y. Shin, D. E. Pritchard, W. Ketterle, Imprinting vortices in a bose-einstein condensate using topological phases. *Phys. Rev. Lett.* 89, 190403 (2002).
- M. J. H. Ku, W. Ji, B. Mukherjee, E. Guardado-Sanchez, L. W. Cheuk, T. Yefsah, M. W. Zwierlein, Motion of a solitonic vortex in the BEC-BCS crossover. *Phys. Rev. Lett.* 113, 065301 (2014).
- S. Donadello, S. Serafini, M. Tylutki, L. P. Pitaevskii, F. Dalfovo, G. Lamporesi, G. Ferrari, Observation of solitonic vortices in Bose-Einstein condensates. *Phys. Rev. Lett.* 113, 065302 (2014).
- Y. Shen, X. Wang, Z. Xie, C. Min, X. Fu, Q. Liu, M. Gong, X. Yuan, Optical vortices 30 years on: OAM manipulation from topological charge to multiple singularities. *Light Sci. Appl.* 8, 90 (2019).
- Y. Margalit, Z. Zhou, S. Machluf, Y. Japha, S. Moukouri, R. Folman, Analysis of a high-stability Stern-Gerlach spatial fringe interferometer. New J. Phys. 21, 073040 (2019).
- L. Amico, M. Boshier, G. Birkl, A. Minguzzi, C. Miniatura, L. C. Kwek, D. Aghamalyan, V. Ahufinger, D. Anderson, N. Andrei, A. S. Arnold, M. Baker, T. A. Bell, T. Bland, J. P. Brantut, D. Cassettari, W. J. Chetcuti, F. Chevy, R. Citro, S. de Palo, R. Dumke, M. Edwards, R. Folman, J. Fortagh, S. A. Gardiner, B. M. Garraway, G. Gauthier, A. Günther, T. Haug, C. Hufnagel, M. Keil, P. Ireland, M. Lebrat, W. Li, L. Longchambon, J. Mompart, O. Morsch, P. Naldesi, T. W. Neely, M. Olshanii, E. Orignac, S. Pandey, A. Pérez-Obiol, H. Perrin, L. Piroli, J. Polo, A. L. Pritchard, N. P. Proukakis, C. Rylands, H. Rubinsztein-Dunlop, F. Scazza, S. Stringari, F. Tosto, A. Trombettoni, N. Victorin, W. Klitzing, D. Wilkowski, K. Xhani, A. Yakimenko, Roadmap on Atomtronics: State of the art and perspective. AVS Quantum Sci. 3, 039201 (2021).

Acknowledgments: We thank the BGU nano-fabrication facility for the high-quality chip and the BGU experimental team for support in acquiring the data. We thank M. Lide, Y. Margalit, D. Rohrlich, Y. Japha, S. Moukouri, and Y. Meir for helpful discussions. Funding: This work was funded, in part, by the Israel Science Foundation (grant nos. 856/18, 1314/19, 3515/20, and 3470/21), the German-Israeli DIP project (Hybrid devices: FO 703/2-1) supported by the DFG, and the European Metrology Programme for Innovation and Research (EMPIR grant 18SIB05 ROCIT). This research was also supported by the Army Research Laboratory under Cooperative Agreement Number W911NF-21-2-0037. Author contributions: Z.Z. did the experiment. R.F. supervised the experiment. S.C.C. performed analytical calculations and numerical simulations. All the authors did the theory, discussed the results, and participated in the writing of the manuscript. C.S., V.S.M., and R.F. supervised the theory and the writing of the manuscript. Competing interests: The authors declare that they have no competing interests. Data and materials availability: All data needed to evaluate the conclusions in the paper are present in the paper and/or the Supplementary Materials.

Submitted 12 July 2024 Accepted 26 March 2025 Published 30 April 2025 10.1126/sciadv.adr6893